Effects of Volumetric Energy Density on Melting Modes, Printability, Microstructures, and Mechanical Properties of Laser Powder Bed Fusion (L-PBF) Printed Pure Nickel

Tianyang Yue [a]†, Zhiyi Zou [b]†, Sheng Zhang [a,*], Haodong Liu [a], Qingyu Chen [a], Wei Wen [c], Yong Zang [a]
a School of Mechanical Engineering, University of Science and Technology Beijing, Beijing, 100083, PR China
b Centre for Additive Manufacturing, University of Nottingham, Nottingham, NG8 1BB, UK
c School of Engineering, Lancaster University, Lancaster, LA14YW, UK

*corresponding author. Tel: 86-15201599409. E-mail address: zhangsheng@ustb.edu.cn

† Equal contribution with the first author

Abstract: Volumetric energy density (VED) is a fundamental criterion for the laser powder bed fusion (L-PBF) process, influencing various forming characteristics. This study employed L-PBF to print pure nickel (Ni) using different VEDs across various melting modes. The thermodynamics in the different melt pools, obtained microstructural features, and tensile properties were characterized and investigated. The results reveal a higher likelihood of keyhole mode melt pool formation than the conduction mode due to the peak temperature exceeding 3005 K. The larger size and slower cooling rate of the keyhole mode melt pool facilitate the formation of cellular subgrains in the central zone and the overall grain coarsening. Compared to the conduction mode, the microstructure in the keyhole mode exhibits a higher dislocation density and a distinct distribution pattern for each type of dislocation. Unlike the L-PBF of commercial Ni alloys, where alloy element distribution significantly impacts tensile performance, the tensile performance of L-PBF Ni is governed by the interaction between grain morphology, dislocation density and distribution.

Keywords: Laser powder bed fusion; Pure nickel; Forming characteristics; Volumetric energy density; Grain morphology; Dislocation

1. Introduction

Pure nickel (Ni) has been widely used in protective components, energy storage devices, and electron devices for aerospace, automotive, and chemical industries owing to its good mechanical properties, outstanding corrosion resistance, excellent high temperature stability, and magnetism [1-4]. Laser powder bed fusion (L-PBF) is a promising powder-bed additive manufacturing (AM) technology. It enables the direct fabrication of metallic components in a layer-by-layer manner [5-

8]. Therefore, it allows more freedom in the product geometry design than conventional manufacturing. In addition, the highly localized energy input associated with the L-PBF process typically leads to rapid melting and solidification. This would result in an ultrafine microstructure and a supersaturated solid solution in the printed Ni, potentially improving its performance [9, 10].

Recent research suggests that near-full density Ni components, with a relative density higher than 99%, can be successfully printed via L-PBF [11-13]. Due to the unprecedented freedom of geometry, the printed Ni can be considered good candidates for heat sinks and protection devices for electronic applications [14, 15]. However, latest research suggests that most of the L-PBF Ni exhibit unsatisfactory properties compared to conventionally manufactured counterparts, including poor ductility, lower wear resistance and corrosion resistance [12, 15, 16]. Many of these can lead to the lack of optimization of the printing process.

Currently, most of the printing process-related research on Ni-based materials is focused on commercial Ni alloys [16-24]. Latest findings suggest that, for such material, different printing processes will affect the precipitation formation and alloy element diffusion in the melt pool, leading to different as-print properties [16-18]. However, these understandings cannot be directly applied to the L-PBF Ni due to the lack of alloy elements in the material. Therefore, significant efforts are still needed to establish the relationship between the printing process of pure Ni, the obtained microstructural features, and the resulting mechanical properties.

Since a layer-by-layer approach was adopted in the additive manufacturing process, volumetric energy density (VED), taking into account the applied layer thickness, is generally considered a way to accurately describe the energy input [25, 26]. Therefore, it has been widely used as a critical index to evaluate the difference in printing processes [25, 27, 28]. As a combined evaluation of multiple process parameters, VED determines the heat transfer, cooling rate, liquid fluidity, and other thermal behaviours during L-PBF process. This directly impacts the most fundamental element of the process, i.e., melting modes of the melt pool [29, 30]. Therefore, it can greatly influence the printability, microstructure, and properties of L-PBF material [17, 18]. As VED varies, there are

mainly two distinct categories of melting modes, the conduction mode and the keyhole mode [18, 31, 32]. At a relatively low input VED, heat conduction is the dominant heat transfer mechanism in the melt pool. This is commonly referred to as the conduction mode melting [18, 33]. The corresponding melt pool is usually small and shallow, with its cross section appearing to be semicircular (i.e., the melt pool depth is less than or equal to its half-width).

In contrast, keyhole mode is observed under a relatively high VED, where heat convection is the dominant heat transfer mechanism [18, 33]. The intense localized heating and vaporization of liquid metals form a deep vapor cavity and generate a recoil pressure in the melt pool. As a result, a keyhole mode melt pool is significantly larger than the conduction mode ones. Its top region is broad because of the radially outward Marangoni flow, which forms a funnel shape. Conversely, its bottom is deep and narrow, resembling a keyhole shape [34, 35]. The corresponding depth of the keyhole mode melt pool is generally larger than the half-width of the melt pool at the top region.

Significant research has been conducted on the influence of different melting modes on the L-PBF of commercially available Ni alloys, mostly IN718, IN738, and IN625 [16-24]. It is generally believed that the conduction mode is more likely to achieve good densification behaviors. Conversely, gas trapped in the bottom of the keyhole melt pool is more likely to introduce porosity defects, resulting in unwanted immature cracking [19-22]. However, research also shows that carefully optimized VED in the keyhole mode regime can successfully suppress the formation of the gas pore porosity, and obtain better ductility or/and strength than the conduction mode printed counterparts and the cast reference [16-18]. It is mainly attributed to the refined and graded microstructure as well as the localized precipitation formation in the melt pool, resulting from the alloy elemental segregation caused by the intense liquid flow in the keyhole mode [16-18]. Meanwhile, the alloy element is more homogeneously distributed in the conduction mode.

However, it should be noted that these well-studied commercial Ni alloys are all heavily alloyed materials, where Ni concentrations are less than 65% [16-24]. Their print behaviors and resulting microstructure should significantly differ from pure Ni and Ni alloy with high Ni concentrations

(>90%), where the influence of alloy elements distribution is minimal. Currently, there is a lack of understanding of how varying VEDs and different melting modes influence the printability, microstructures, and final mechanical properties of L-PBF Ni.

Based on above, this study applied a wide range of VEDs to print Ni to explore the varieties of melting modes. The objective was to better understand the solidification behaviors in the L-PBF Ni melt pool under different VEDs and melting modes, and try to establish the relationship between the applied VEDs and resulting microstructure and mechanical properties. In this study, the resulting relative density and surface morphology were characterized to evaluate the corresponding printability. The differences in the obtained microstructures were analyzed, and the corresponding relationship between the microstructure and tensile behaviors was also examined and discussed.

2. Materials and methods

2.1 Materials and the L-PBF process

Gas-atomized spherical Ni powders, as shown in Fig. 1, with particle sizes distributed between 5 to 100 μm and a mean diameter of 35.80 μm, were used in this study. Their composition is reported in Table 1.

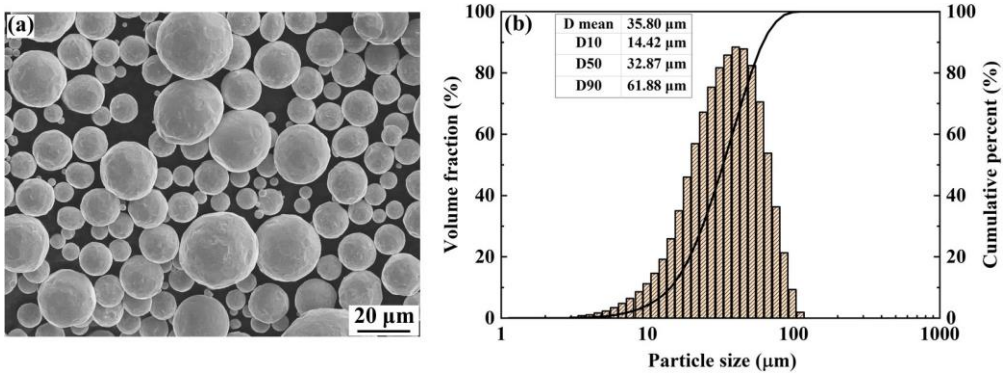

Fig. 1. Characteristics of Ni powders: (a) the morphologies and (b) the particle size distribution.

Table 1 Chemical composition of Ni powders used in this study measured by inductively coupled plasma (ICP).

Elements	Ni	Mn	C	Si	S	Fe	Cu
wt %	bal.	0.016	0.02	0.012	0.001	0.002	0.003

An EOSINT M280 system with a 400 W Ytterbium fiber laser was used to print the Ni powder. Before the printing, the substrate was preheated to 80 ℃, and the O_2 concentration in the process chamber was limited to a value below 500 ppm by being flushed with Argon. The schematic diagrams of the L-PBF processing are shown in Fig. 2(a), where the laser scanning direction was rotated by 67° between adjacent layers to minimize the internal residual stress. The detailed process parameters used in this study are shown in Table 2. Various laser power and scanning speed were chosen to adjust the VED. A hatching distance of 90 μm can create a certain level of overlap between scan hatches, which is believed to help reduce the formation of defects. Layer thickness was kept constant as 40 μm according to the average size of powders. Based on the applied process parameters, the corresponding VED can be calculated by equation (1) [36]:

$$\eta = \frac{P}{\upsilon h t} \tag{1}$$

where η is the VED, P is the laser power, υ is the scanning speed, h is the hatching space, and t is the layer thickness. Therefore, the applied VED ranges from 41.15 to 240.10 J/mm3 in this study. This wide range of the VED guarantees the obtaining of various melting models.

Table 2 L-PBF processing parameters for all parts.

Processing parameters	Applied Values
Laser powers, W	200, 250, 300
Scanning speed, mm/s	350, 450, 550, 650, 750, 850, 950, 1050, 1150, 1250, 1350
Hatching space, μm	90
Layer thickness, μm	40
Spot size, μm	100
Volumetric energy density, J/mm^3	41.15-240.10
Laser rotation angle	67°

Two types of samples, i.e., blocks and tensile samples, were printed in this study, as shown in Fig. 2. The printed block samples with a size of 8×8×10 mm were used to assess the relative density (RD) and surface quality. The blocks were then wire cut along the build direction on the top surface to expose the melt pool on the first layer of the printed material (Fig. 2(b)). Thick plates with tensile specimen contour were printed parallel and perpendicular to the building direction, and then were

wire cut to a batch of 3mm thick tensile specimens with a gauge length of 40 mm (Fig. 2(c)), according to ASTM E8 standard. The actual specimens of blocks and tensile plates are shown in Fig. 2(d) and (e). For comparison, tensile specimens with the same dimensions were also machined from the conventionally manufactured casting material as the reference.

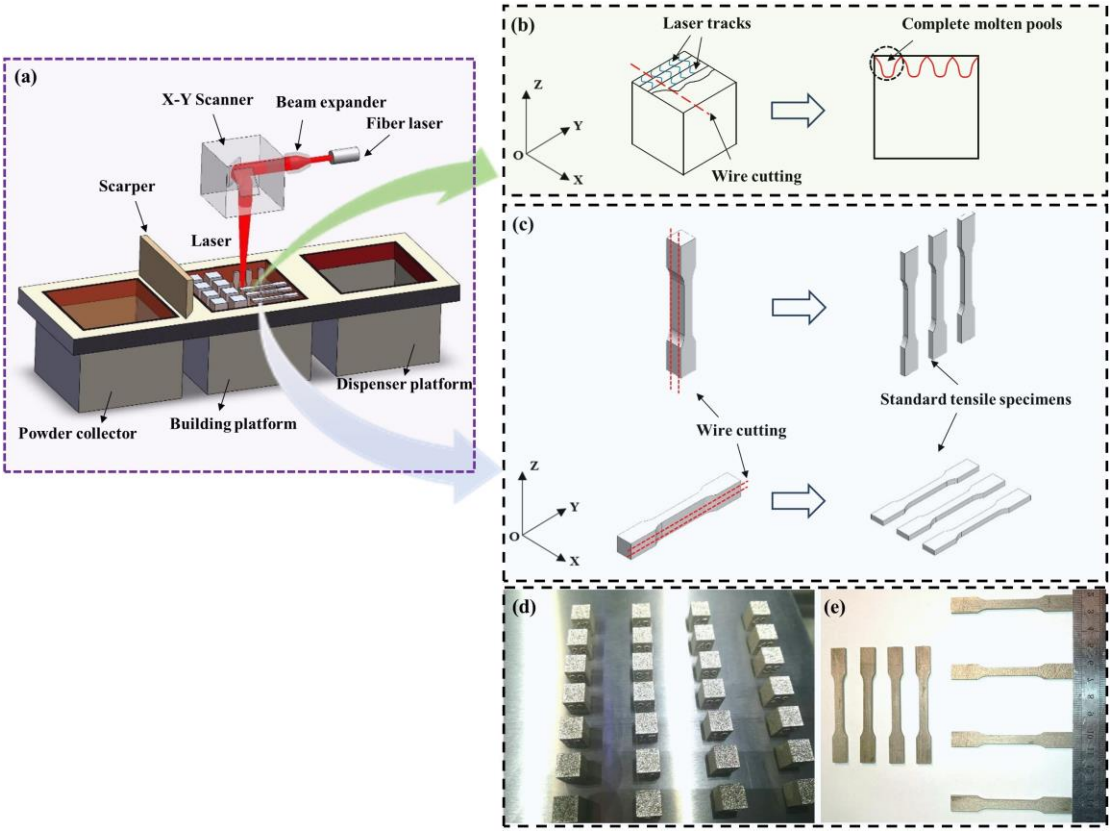

Fig. 2. Schematic diagrams showing the L-PBF system: (a) L-PBF processing, (b) blocks fabrication, (c) tensile samples fabrication, (d) blocks samples, (e) tensile samples.

2.2 Microstructural characterization

Before microstructural characterization, the printed material was mirror-polished and then etched for about 10 seconds in a corrosive reagent (2 ml H_2O + 10 ml HNO_3 + 10 ml $C_2H_4O_2$) at room temperature to reveal the obtained microstructure. The exposed melt pools were observed via an optical microscope (OM, Zeiss Axio Imager 2, Germany) from the first scanned layer on the top surface. The width and depth of melt pools were measured on the optical images using Image J software. Its aspect ratio, i.e., Depth/Width (D/W), is calculated to distinguish the melting modes. A ratio less than 0.5 is recognized as the conduction mode, while greater than 0.5 is recognized as the keyhole mode. The RD of as-printed material was also measured via image analysis of the

optical images. The resulting porosity ($A_{porosity}$) of each image was quantified using Image J, and six optical images of the same printing condition were used to the average $A_{porosity}$. Then RD could be obtained from equation (2):

$$RD = \left(1 - A_{porosity}\right) \times 100\% \quad (2)$$

The surface morphology and detailed as-printed microstructures were observed using a scanning electron microscope (SEM, FEI Quanta 650 FEG, America) on the top surface of the samples. Energy dispersive spectrometry (EDS, Esprit Compact, USA) was applied to characterized element distribution in specimens. The textures of the as-printed samples were characterized using an electron back-scattered diffraction (EBSD, EDAX Hikari Plus, USA) detector in the SEM. Before the EBSD characterization, the polished specimens were further electrolytically polished in a mixture of 10 ml $HClO_4$ (10 pct) and 90 ml C_2H_5OH at a voltage of 5 V for 20 s to remove deformation surface and stress concentration.

2.3 Tensile testing

A CMT5105 (China) testing machine was used to measure the yield strength (YS), ultimate tensile strength (UTS), and elongation (EL) of the as-printed and as-cast samples at room temperature with a cross-head velocity of 1 mm/min. A dynamic strain gauge extensometer was applied to record the engineering strain during the test.

2.4 Finite element analysis

To better understand the thermodynamics in the melt pool under different melting modes, finite element analysis (FEA) was employed, referencing previous studies [37-40]. This analysis studied the fluid dynamic of the molten liquid during the L-PBF process. A computational fluid dynamics (CFD) model was applied using ANYSY FLUENT software. Detailed model descriptions and related material physical properties are summarized in the **Supplementary material**.

3. Results

3.1 The formation of different melting modes

The microstructure of the printed samples observed from the side surface (XZ plane) is displayed

in Fig. 3. The melt pool morphology under each condition can be clearly identified from the top layer, as plotted by the white dashed lines. It is evident that the morphology of the melt pool varies within the process window, and is VED dependent. Similar VED will result in similar melt pool morphology, considering the combination of laser power and scan speed. Therefore, VED can be considered the criterion for distinguishing the melt pool morphology and melting mode.

The depth, width, and D/W of each melt pool are measured and plotted in Fig. 4(a). It can be found that these values exhibit an increasing trend with the increase of VED. When the VED was less than 52 J/mm^3, the width ranged from 60 to 103 μm and the depth was less than 36 μm. These relatively small values resulted in a low D/W ratio (<0.4). When the VED increased to 52–67 J/mm^3, the width fluctuated in the range of 98–114 μm, and the depth ranged from 36 to 54 μm. Consequently, there was a slight increase in the corresponding D/W ratio, mostly in the range of 0.4-0.5. As shown in Fig. 4(b), these melt pools exhibited an approximately oval shape due to the small D/W ratio. As the VED continued to increase, the depth gradually approached the width, causing the D/W ratio to exceed 0.5. The D/W ratio finally reached to or even surpassed 1 when the VED exceeded 152 J/mm^3. In addition, the melt pool morphology changed significantly due to the increased depth, particularly when the VED approached or exceeded 100 J/mm^3. The shape of melt pools was wide on top and narrow on bottom, resembling a funnel. According to previous studies [18, 33], melt pools with a D/W ratio less than 0.5 are typically defined as the conduction mode, while those with a ratio exceeding 0.5 are defined as keyhole mode, as shown in Fig. 4(b). Therefore, it can be concluded that within the process window, the melting modes for L-PBF Ni are tend to be more inclined toward the keyhole mode.

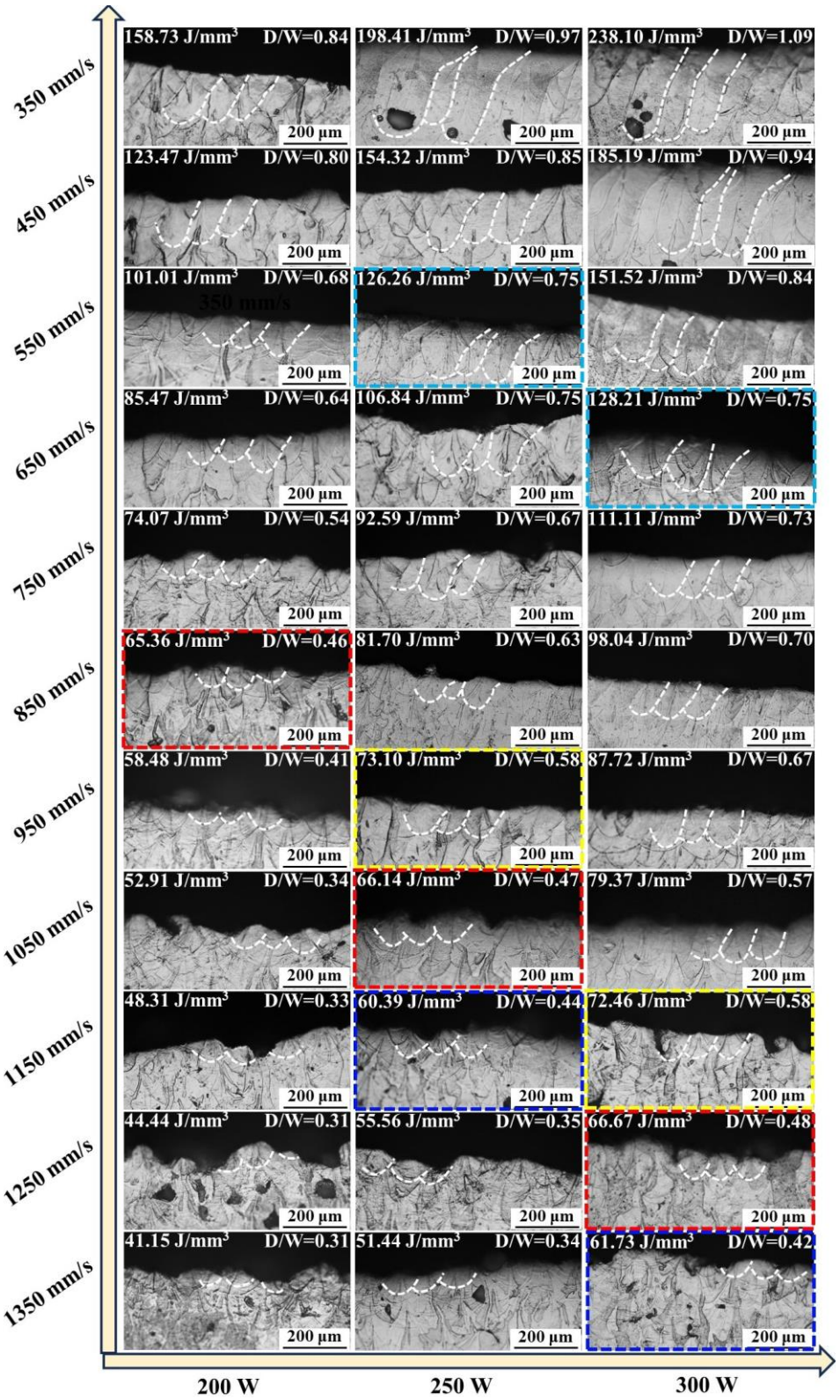

Fig. 3. The microstructure of the printed samples observed from the side surface (XZ plane).

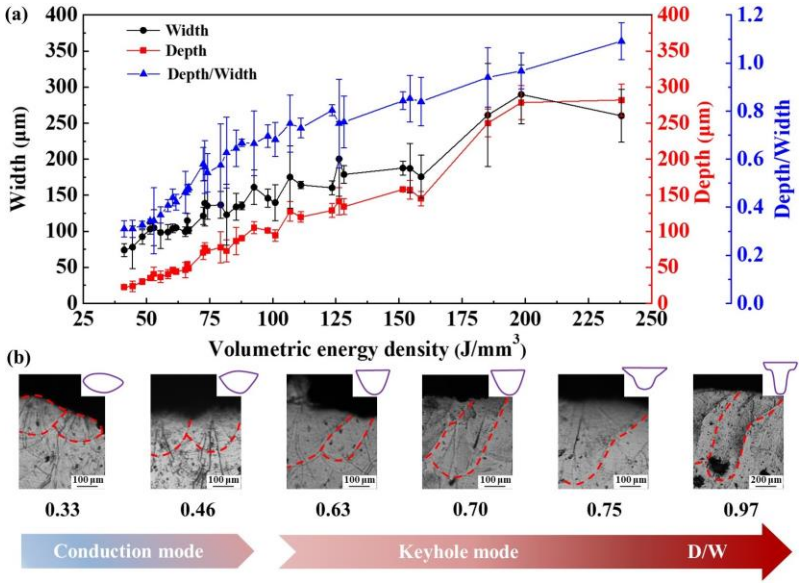

Fig. 4. (a) Width, depth and depth/width of melt pools, (b) Schematic diagram showing the change of melting modes.

3.2 Densification behaviours under different melting modes

It is known that L-PBF printing is a process of accumulation of melt pools. Therefore, the densification behaviors and surface morphologies highly depend on the quality and features of the melt pools [17, 41]. The features of melt pools were primarily associated with VED within the process window as shown in Fig. 3. Therefore, the relationship between the RD of specimens and VED was plotted as shown in Fig. 5. Meanwhile, the polished cross-sections of the specimens are shown in Fig. 6.

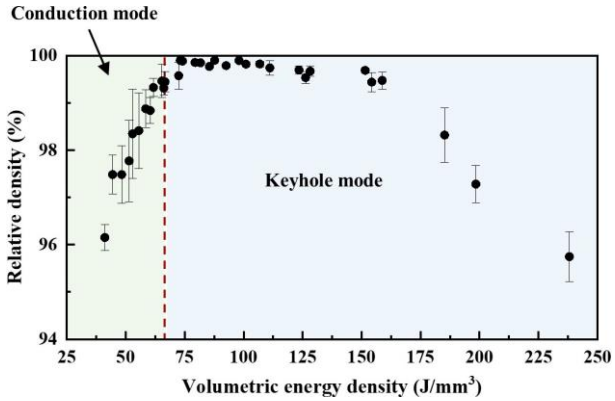

Fig. 5. Relative density of as-printed samples under different VEDs.

It could be found that the RD increased first and then decreased with increasing VED. When the VED<67 J/mm^3, i.e., in conduction mode, most RD values fluctuated in a low range of 96.15-98.84 %. Only a few specimens had an RD above 99% but all were below 99.5%. It was attributed

to the large number of pores in the specimens, as shown in Fig. 6(a1) and (a2). These pores were in irregular polygonous shapes, and some of them had a large size of over 100 μm. Besides, some completed unmelted powders in the pores could be observed by SEM (Fig. 6(b1) and (b2)), showing a typical characteristic of lack of fusion defects [42, 43]. The melt pool in conduction mode had a small width and depth as seen in Fig. 3 and 4. This caused insufficient overlap between adjacent laser tracks or layers as shown in Fig. 6(b3). Furthermore, such a feature led to the lack of fusion. With the increase of VED, the melt pools became wider and deeper. Therefore, the overlaps would be sufficient enough to eliminate the serious lack of fusion in the specimens as shown in Fig. 6(a5) and (a6). This ultimately resulted in an improved RD. Therefore, the keyhole mode exhibited a higher RD of 95.75-99.90%. Particularly, no obvious pores and defects can be observed when the VED was below 99 J/mm^3, resulting in an RD exceeding 99.5%. Although there was no lack of fusion defects in the specimens under higher VED, nearly circular pores can be observed instead, as shown in Fig. 6(a7) - (a12). Particularly, the serious circular pores occupied the specimens when the VED exceeded 152 J/mm^3, resulting in a lower RD (95.75-98.32%). Those nearly circular pores with internal gas flow channels at the bottom of the melt pool exhibited remarkable characteristics of keyhole defects as shown in Fig. 6(c1) - (c3) [43, 44].

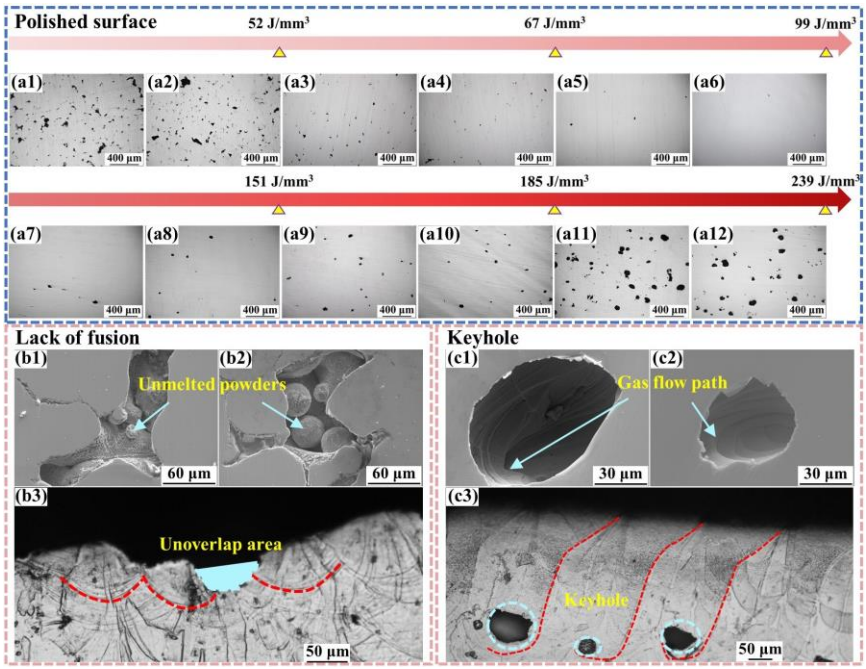

Fig. 6. (a1) - (a12) Polished cross-sections of the specimens, (b1), (b2) SEM images of lack of fusion, (b3) High-magnification metallographic images of melt pools under the VED of 48.31 J/mm^3, (b1), (b2) SEM images of keyhole, (b3) High-magnification metallographic images of melt pools under the VED of 198.41 J/mm^3.

To better classify the densification behaviors of different samples, the relationships between the process window and densification behaviors were also established, as shown in Fig. 7. It can be noted that only a small fraction of the conduction modes can achieve an acceptable RD (99-99.5%). This indicated that the specimens had good printability but still had a small number of pores with tiny sizes. As a comparison, nearly four-fifths of keyhole mode possessed the excellent RD (>99.5%), indicating that the specimens had superior printability without apparent pores. Only three samples with keyhole modes showed poor printability (RD<99%), characterized by severe keyhole defects. Therefore, it can be concluded that the keyhole model was more favorable in L-PBF printing of Ni.

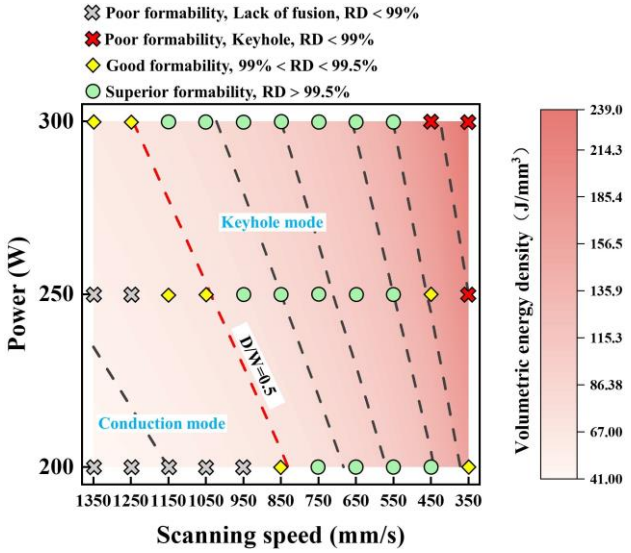

Fig. 7. Relationships between the process window and densification behaviours of printed specimens.

3.3 The obtained subgrains in different melting modes

Four representative samples, i.e., good RD specimens with different melt pool morphology, are selected to observe the subgrains in the melt pools, as shown in Fig. 8. The melt pool boundaries are marked by white dashed lines. Both the melt pool boundary region and the central zone are observed under high magnification SEM. The results show two main subgrain structures in the melt pools: columnar structures and cellular structures. Notably, the size of cellular structures approaches the width of columnar structures since the cellular structures are commonly known as the cross-section of columnar structures [45]. Both the central zone and boundary region in conduction modes primarily consist of columnar structures as shown in Fig. 8(a). However, although the boundary region in keyhole modes is still columnar structures, the central zone is dominated by cellular

structures, as shown in Fig. 8(b)-(d). In addition, the columnar structures in the keyhole modes are significantly coarser than those in the conduction modes. Image analysis on multiple microscopy photos of the boundary region suggests that the width of columnar structures in conduction modes is only around 370 nm, whereas in keyhole modes it becomes more significant with a size that exceeds 800 nm, as shown in Fig. 8(d). In addition, Fig. S2 shows the EDS maps of the subgrain under different melting modes, which indicates a lack of noticeable oxide particles as mentioned in previous studies [46-48]. This is due to the strict control of oxygen content below 500 ppm, which reduces the oxidation of specimens during L-PBF process. Additionally, research suggests that the oxide particle commonly exists in the form of precipitates in conjunction with other elements [46, 47]. The very small amounts of impurity elements in Ni make it difficult make it difficult to precipitate, thereby preventing the formation of oxidized precipitates.

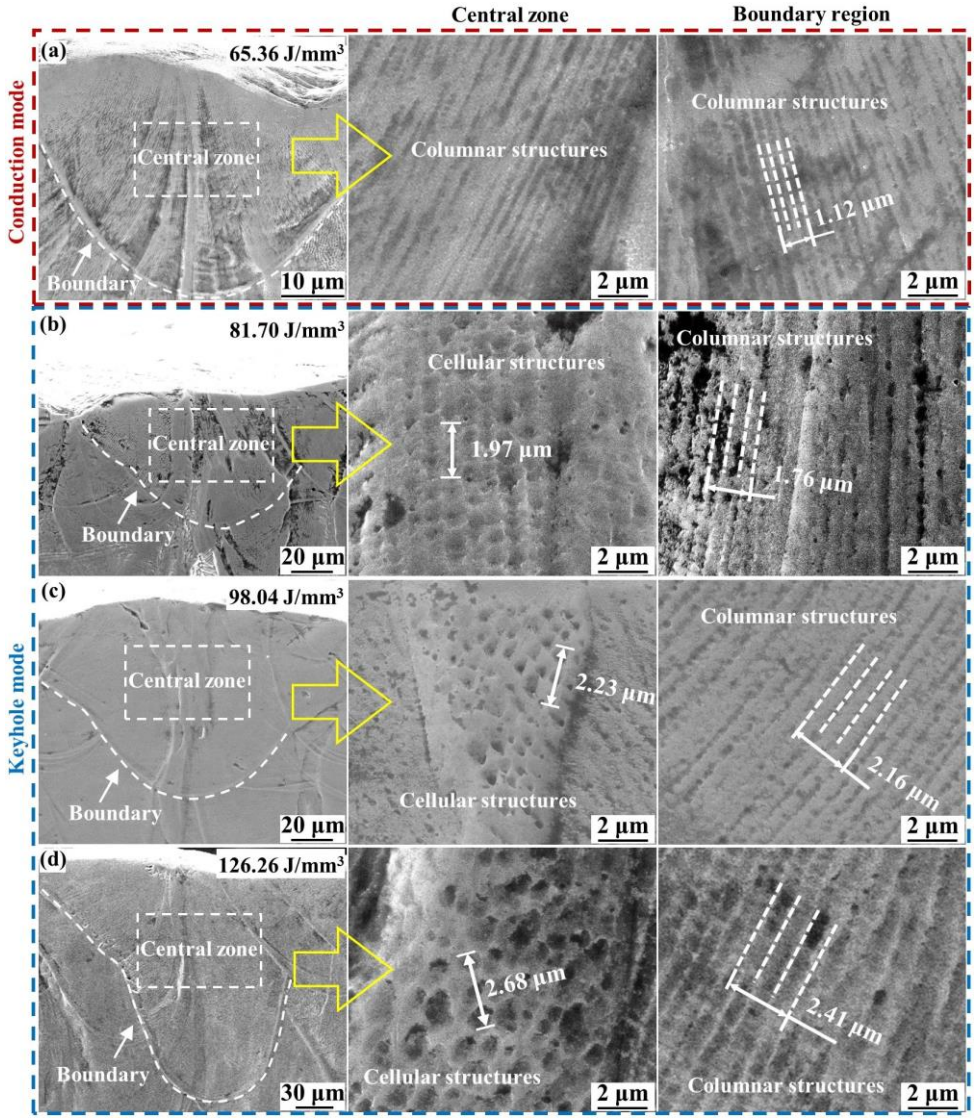

Fig. 8. High magnification SEM of the subgrains in melt pool boundary region and the central zone.

3.4 The obtained texture in different melting modes

The textures of the various as-printed samples, including inverse pole figure (IPF) maps and pole figure (PF) maps, are shown in Fig. 9. The IPF maps revealed that plenty of slender columnar grains were formed along the building direction. Therefore, the grains exhibited an equiaxed morphology on the top surface. A {001} texture could be identified in the conduction mode. However, the texture was weak, as suggested by the low maximum texture intensity (2.102). Besides, columnar grains exhibited a weak preferred orientation along <001> crystallographic direction. With increasing VED, the texture transformed into a strong {110} texture with the texture intensity increasing from 6.014 to 10.512. An intensified preferred orientation in <101> direction was also observed in the keyhole mode.

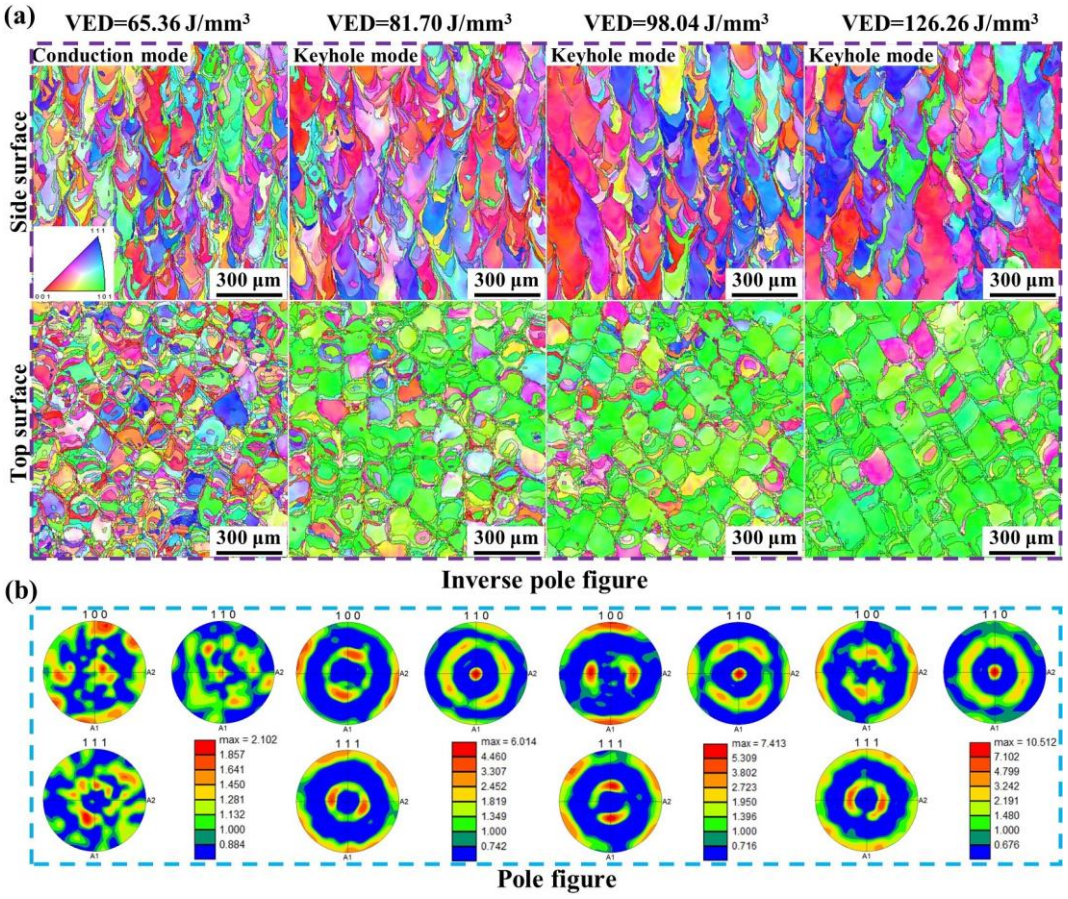

Fig. 9. Texture of the various as-printed samples, including inverse pole figure (IPF) maps (a), and pole figure (PF) maps (b).

In addition, it can be observed that the grains became larger with the increase of VED, resulting in coarser grains in keyhole mode than those in conduction mode. The average grain size can be

calculated from the EBSD results, as shown in Table 3. The average grain size on the top surface and from the side surface in conduction mode was about 40 μm and 61 μm, respectively. However, the average grain size was calculated to be 85 μm and 131 μm from the top surface and side surface when the keyhole mode samples formed under the VED of 126.26 J/mm^3. This size is more than twice the size of the conduction mode, indicating relatively small amounts of grain boundaries.

Table 3 Grain size in different surfaces of samples formed under different VEDs.

VED (J/mm^3)	Top surface (μm)	Side surface (μm)
65.36	40.00±26.6	61.07±37.8
81.70	63.33±40.3	81.28±46.2
98.04	72.97±44.5	113.03±82.0
126.26	84.66±49.2	130.57±79.5

The misorientation distribution at the grain or sub-grain boundary is plotted in Fig. 10(a). Boundaries with a misorientation of less than 15° are classified as low-angle grain boundaries (LAGBs), marked by red lines (2-5°) and green lines (5-15°). Boundaries with a misorientation greater than 15° are classified as high angle grain boundary (HAGBs), marked by blue lines (15-60°) [20, 32]. It can be noted from Fig. 10(a) that the distribution of red lines and green lines becomes denser with the increase in VEDs, regardless of the surface under observation. This indicates an increasing trend in the fractions of LAGBs as the applied VED increases. Such observation is further supported by the distribution histogram of the misorientation angle (Fig. 10(b)). The fraction of LAGBs is approximately 40% at both surfaces with a VED of 65.36 J/mm^3. However, the fraction exceeds 60% with a VED of 126.26 J/mm^3.

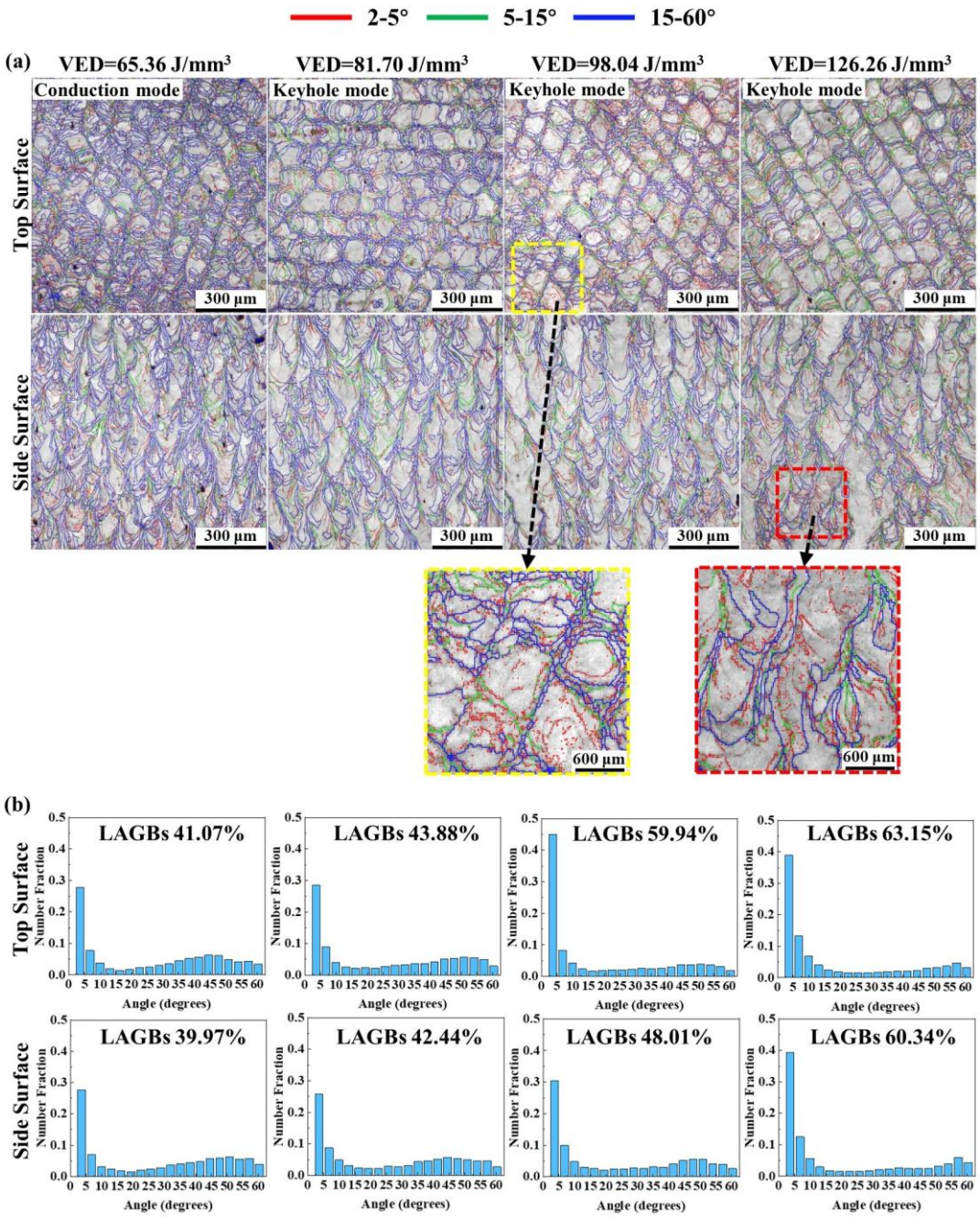

Fig. 10. (a) Misorientation maps of the L-PBF Ni fabricated under different VEDs, (b) distribution histogram of misorientation angle.

Furthermore, the enlarged insert image in Fig. 10(a) shows a significant presence of red lines within the columnar grains, indicating the accumulation of subgrain boundaries (SGBs) [49]. The fraction of the SGBs also exhibits an increasing trend as VEDs increase. The fraction of SGBs is approximately 27% at a VED of 65.36 J/mm^3, but increases to 38% at the VED of 126.26 J/mm^3. The formation of intensive SGBs also contributes to the overall increase of LAGBs.

Previous research suggests that the LAGBs are commonly linked to the formation and movement of dislocations [50]. Dislocations in a crystalline metal are generally stored as geometrically necessary dislocations (GNDs) and statistically stored dislocations (SSDs) [51-53]. GNDs are accumulated in the strain gradient fields [51, 52]. They can be characterized using the kernel average misorientation (KAM) method [43, 44], as shown in Fig. 11. The presented KAM maps suggest that the GNDs are relatively homogeneously distributed across the grain and melt pool under low VED located in the conduction mode region (Fig. 11(a)). In contrast, with a higher VED located in the keyhole mode region, the GNDs are mainly concentrated around the grain boundary and melt pool boundary. The average GNDs density from the KAM maps is shown in Fig. 11(b), illustrating that a higher VED would result in a high GNDs.

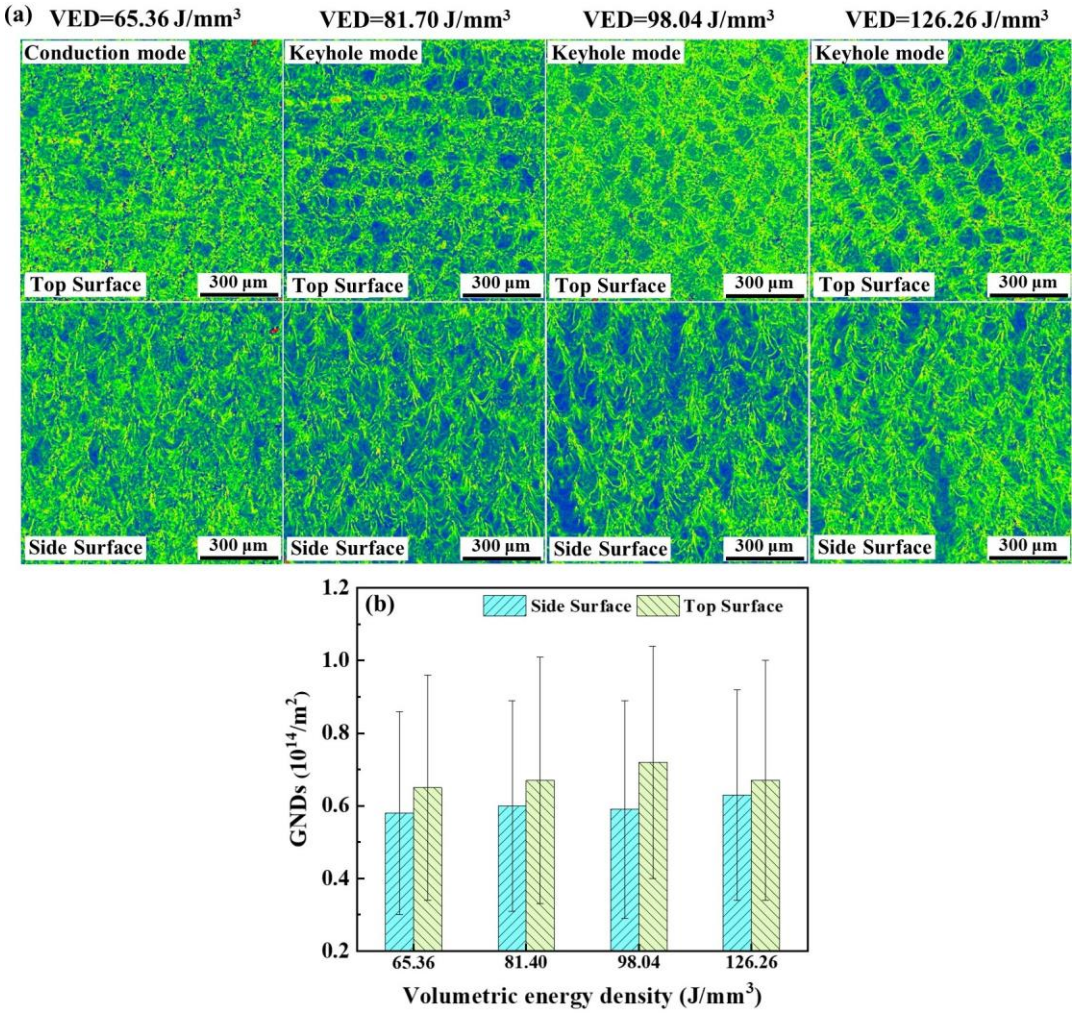

Fig. 11. (a) KAM maps of the L-PBF Ni fabricated under different VEDs, (b) corresponding GNDs from (a).

On the other hand, SSDs are generally accumulated during uniform plastic straining [51, 52]. It is

widely accepted that the deformed area of the microstructure can be identified as the area with a grain orientation spread (GOS) value larger than 2° [50, 54]. The GOS maps obtained from the EBSD analysis are shown in Fig. 12(a) and (b), with the deformed area highlighted in blue. The GOS maps reveal that the L-PBF microstructure is characterized by the deformed texture. A higher VED would result in a higher area fraction of the deformed region, as shown in Fig. 12(c). Due to the increase in the deformed region, it is reasonable to believe that a high VED would also lead to an increased density of SSDs. Since the KAM results in Fig.11 already showed that GNDs also tend to be higher with a high VED, it can be concluded that the dislocation density in samples under high VED, namely in keyhole mode, is higher than that that under the conduction mode.

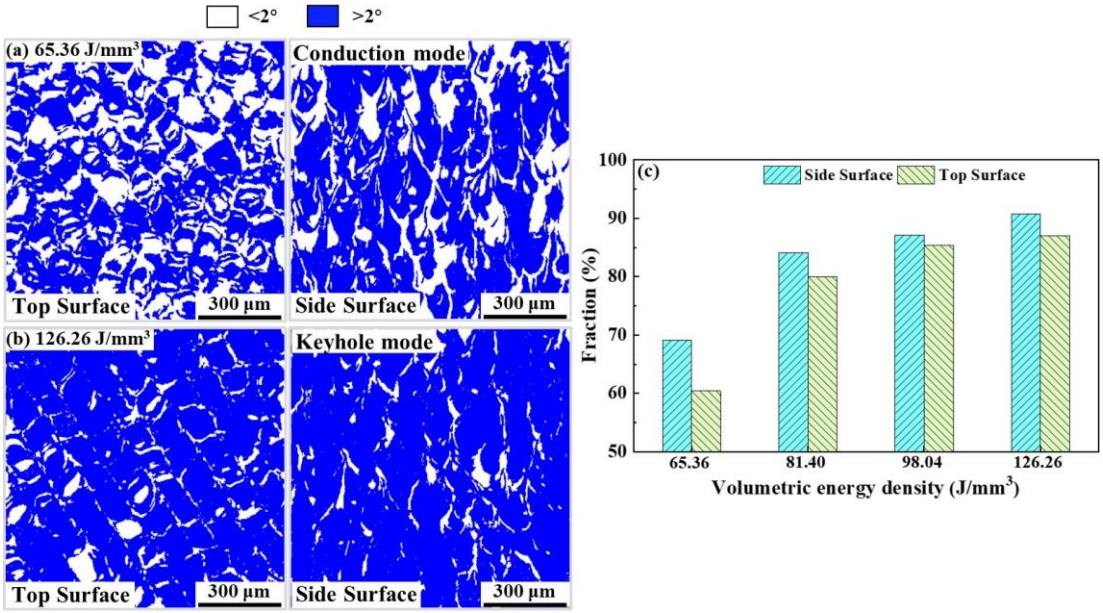

Fig. 12. (a) and (b) GOS maps of the L-PBF Ni fabricated under different VEDs, (c) fraction of deformed grains.

3.5 The obtained tensile properties in different melting modes

The typical true tensile stress-strain curves of as-printed samples fabricated perpendicular and parallel to the building direction are shown in Fig. 13, with the tensile properties of as-cast samples listed as a reference. Besides, detailed values of YS, UTS, and EL are reported in Table 4. It is evident that the as-printed samples have achieved excellent mechanical strengths, particularly in terms of the YS. It reached the range of 284.1–291.1 Mpa and 239.5–264.6 Mpa, respectively, much better than that of as-cast samples (93.11 Mpa). It can also be found that the conduction mode

commonly exhibited a larger YS compared to the keyhole mode, particularly when the samples were printed parallel to the building direction. However, the EL of as-printed samples fluctuated violently. The EL of samples fabricated perpendicular to the building direction increased from 28.5% to 41.6% with increasing VED, and the EL (28.5%) of conduction mode samples was far below the EL (40.5%) of as-cast samples. In contrast, EL notably improved when samples were printed parallel to the building direction. The EL in conduction mode reached 37.5%, while in keyhole mode achieved 58.9–59.5%, which has an improvement of ~50% compared to as-cast samples.

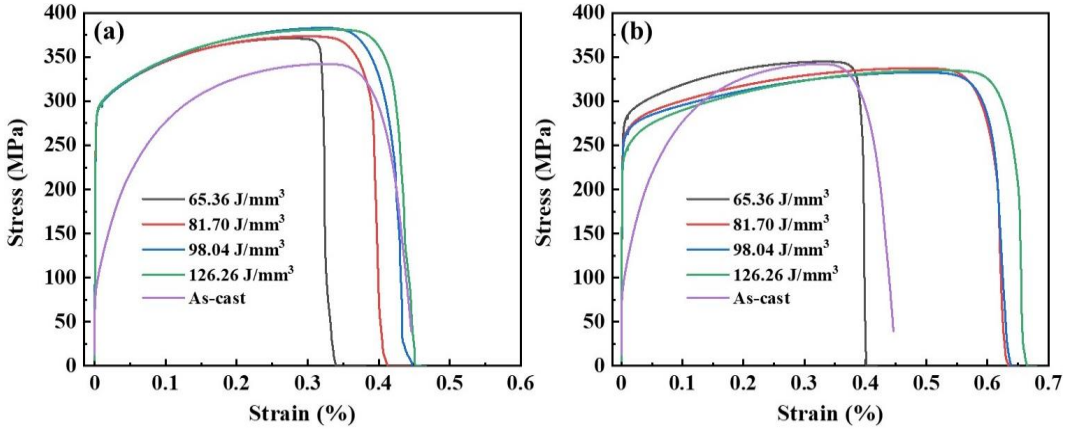

Fig. 13. Typical stress-strain curves of as-printed samples and as-cast samples: (a) as-printed samples fabricated perpendicular to the building direction, (b) as-printed samples fabricated parallel to the building direction.

Table 4 Tensile properties of as-printed samples and as-cast samples.

Processing condition		VED (J/mm^3)	YS (MPa)	UTS (MPa)	EL (%)
As-printed	Perpendicular to the building direction	65.36	290.0±8.9	370.5±1.0	28.5±1.1
		81.70	288.5±3.9	379.1±5.0	38.8±1.1
		98.04	291.1±7.4	392.7±10.7	40.2±2.8
		126.26	284.1±2.4	381.8±0.6	41.6±0.6
	Parallel to the building direction	65.36	264.6±5.8	347.7±4.6	37.5±2.3
		81.70	252.6±8.8	336.2±6.2	59.3±4.8
		98.04	246.0±11.2	330.3±7.5	59.5±3.6
		126.26	239.5±10.6	338.3±7.3	58.9±3.4
As-cast		—	91.0±2.9	341.2±1.6	40.5±2.5

It can be found that the tensile properties, including UTS and YS, of as-printed Ni are close to or even surpass those of as-cast Ni, especially for the as-printed samples fabricated perpendicular to the building direction. However, not all the as-printed samples exhibit a good EL as as-cast samples.

The conduction mode, whether fabricated parallel to or perpendicular to the building direction, demonstrates lower EL than the as-cast sample. In comparison, keyhole mode can significantly improve the elongation of as-printed samples. Specifically, the EL approaches that of as-cast samples when as-printed samples are printed perpendicular to the building direction, and much higher when printed parallel to the building direction.

The results illustrate that the keyhole mode can achieve a better combination of tensile properties and ductility of as-printed Nis than the conduction mode, which is almost comparable to as-cast Ni.

4. Discussions

4.1 Effect of VED on the formation of melting modes

Results in section 3.1 suggest a close correlation between the melting mode and the VED. This correlation is widely believed to result from different thermodynamic behaviors of the molten liquid under different laser energy inputs [31, 41]. To gain a deeper understanding of this correlation mechanism, simulations of liquid behaviors in various melt pool environments were conducted. The results are shown in Fig. 14, which illustrates the temperature distribution within and around the melt pool, as well as the corresponding velocity of each fluid element in the melt pool.

It can be noticed that the peak temperature in the keyhole mode is significantly higher than that of the conduction mode, leading to a larger volume of the molten liquid and, subsequently, a larger melt pool size.

At a relatively low energy input, such as the VED of 48.31 J/mm^3 shown in Fig. 14(a1) and (b1), the Ni is insufficiently melted in the melt pool. Therefore, the unmelted particles will lead to poor fluidity of the liquid and result in a low wettability between the liquid and the substrate, causing evident defects like open pores and humps [43, 55]. This result was consistent with the laser tracks shown in Fig. 14(c1), where the blocks consist of these melt pools shows a coarse surface morphology. With VED increasing to 65.36 J/mm^3, as shown in Fig. 14(a2) and (b2), powders are fully melted, making the molten liquid phase easy to flow and wet the substrate. As a result, defect morphologies in the laser track are efficiently restrained. As a result, defect morphologies in the

laser track are efficiently restrained, as shown in Fig.14(c2). It can also be noted that the liquid moves slowly and steadily under this condition, without any noticeable recoil movement. This feature contributes to the formation of the shallow and hemispherical morphology of the typical conduction mode melt pool.

As the VED moves into the keyhole mode region, as shown in Fig. 14(a3) - (a6) and (b3) - (b6), much more powders are melted. This results in a larger size of the melt pool than that of the conduction mode, with further improved fluidity and wettability. The laser tracks become regular and smooth, as shown in Fig. 14(c1) - (c6). Meanwhile, the temperature of the core of the molten liquid starts to exceed the material's boiling point (3005K for Ni) due to the excessive energy input. Therefore, the evaporation of liquid metal occurs, and a recoil pressure is produced. Such a recoil pressure can push the liquid materials to flow deeper into the pre-deposited region [56], as shown in Fig. 14(d2) - (d4). Additionally, the excessive heat will also be transferred to the pre-deposited region to further remelt the material. Thus, a deeper melt pool is formed.

These melt pools with larger sizes are tightly bonded to each other, as shown in Fig. 3, eliminating the lack of fusion porosity. However, when the evaporation is drastic, recoil pressure can push liquid materials to form a cavity at the bottom of deep melt pools, as shown in Fig. 14(b6) and (d4). Once the cavity collapses and there is no sufficient time for the trapped gas to escape from the melt pools before the solidification, keyhole defects can be formed [7, 27, 56].

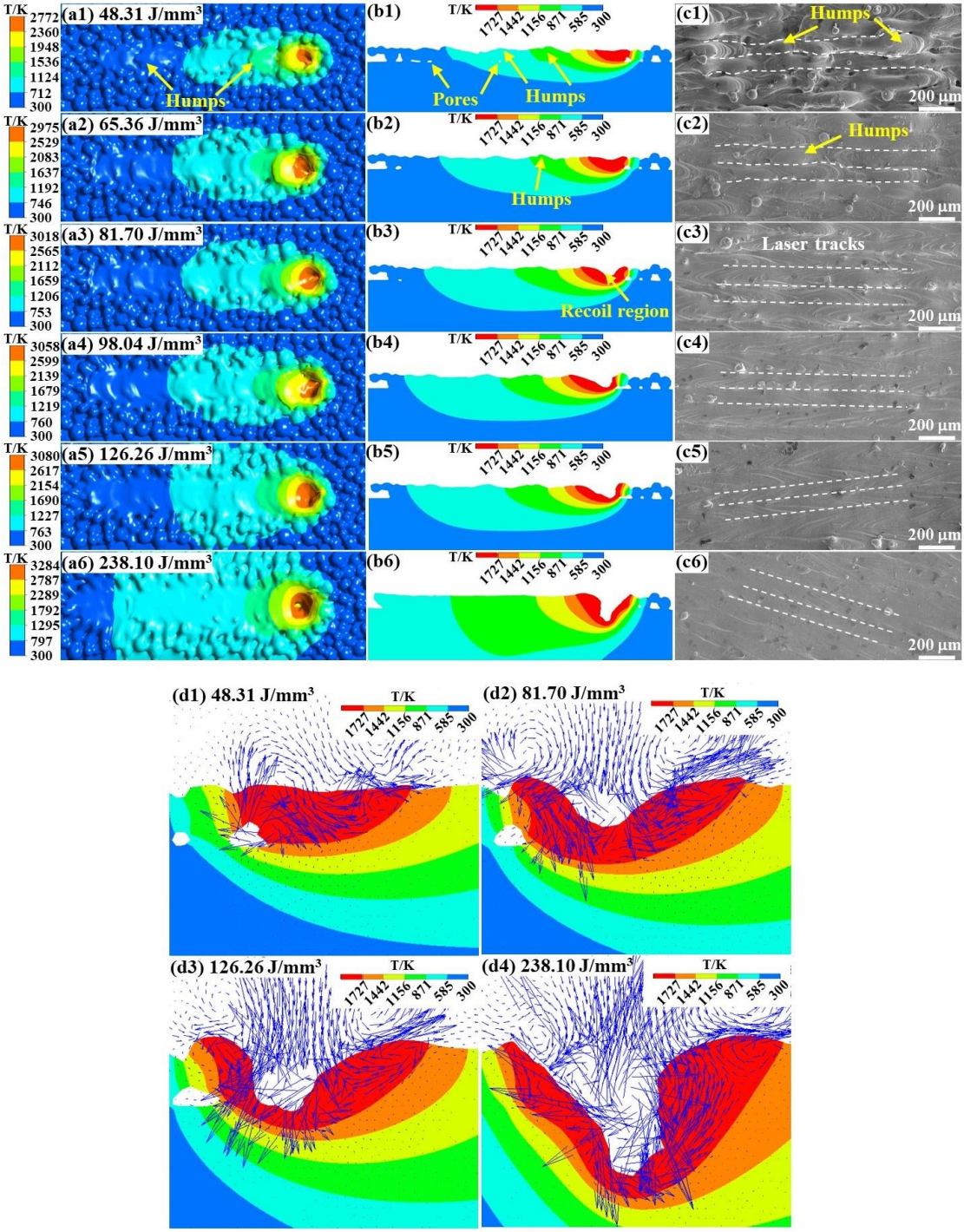

Fig. 14. Liquid behaviours under various melt pool environments, (a) Top views of temperature field, (b) Longitudinal sections of temperature field, (c) laser tracks on blocks, (d) velocity evolution of fluid in melt pools.

4.2 Effect of melting modes on the microstructure evolution

Due to the layer-wise building method of the L-PBF process, heat in the melt pool is usually transferred directionally from top to bottom, parallel to the building direction. This directional heat

transfer contributes to forming dominant columnar grains in the as-printed material [57, 58], regardless of the applied VED. However, it can be found that grain size, clustering of dislocation, and preferred orientation vary with the different melting modes. This is the result of the different thermal behaviors in the two melting modes [16-18].

Section 3.3 and section 3.4 evidence that different subgrain morphology and types of dislocations are formed in the L-PBF Ni linked to the applied VED and melt pool locations. These microstructural features indicate different heat dissipation capacities under different conditions. Columnar structured subgrains result from the directional growth of nuclei following a high thermal gradient, while cellular structured subgrains are formed due to the epitaxial growth of nuclei in a relatively lower thermal gradient [59, 60]. Meanwhile, GNDs are accumulated in the high strain gradient fields, resulting from a high thermal gradient in the context of the L-PBF process [51, 52]. In contrast, the SSDs are concentrated in regions with relatively smoother temperature changes.

To analyze the thermal gradient under different conditions more effectively, the temperature distribution within different melt pools is FE simulated and reported in Fig. 15. Fig. 15(a) demonstrates that the melt pool in the conduction mode has a small size, and the limited heat dissipation distance from the central zone to boundary region would induce a large thermal gradient in this small region. Therefore, the columnar subgrain structures dominate the conduction mode melt pools, with an even distribution of the GNDs.

In contrast, the melt pool in keyhole mode exhibits a large melt area, as shown in Fig. 15(b). Therefore, the well-surrounded central zone would have an extended heat dissipation distance and a reduced thermal gradient. This creates a region with a more homogenized temperature distribution, where the cellular subgrains and SSDs can be formed and accumulated. Furthermore, the existence of such a homogenized high-temperature region deviates the heat dissipate direction, thus altering the preferred orientation of the columnar correspondingly.

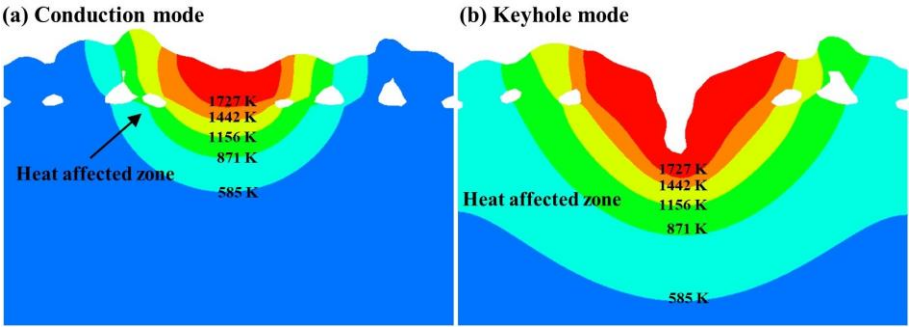

Fig. 15. Cross sections of temperature field under different melting modes, (a) conduction mode, (b) keyhole mode.

In addition, the large keyhole melt pool induces a more extensive heat-affected zone, as shown in Fig. 15(b), and a longer cooling time [37]. It further slows down the cooling of the melt pool. The FE computed temperature profile at the specified location of different melt pools is plotted in Fig. 16. Point 1 is located in the central zone of the melt pool, while point 2 and point 3 are in the boundary of the melt pool. It reveals that although a keyhole melt pool exhibits a higher peak temperature, its cooling rate is lower compared to the conduction mode, with a higher VED corresponding to a lower cooling rate (Fig. 16(d) - (f)). Such a trend aligns well with the experimental discoveries [6]. The relatively slowed cooling prolongs the growth time of subgrains, resulting in the formation coarser grains in the keyhole mode [61].

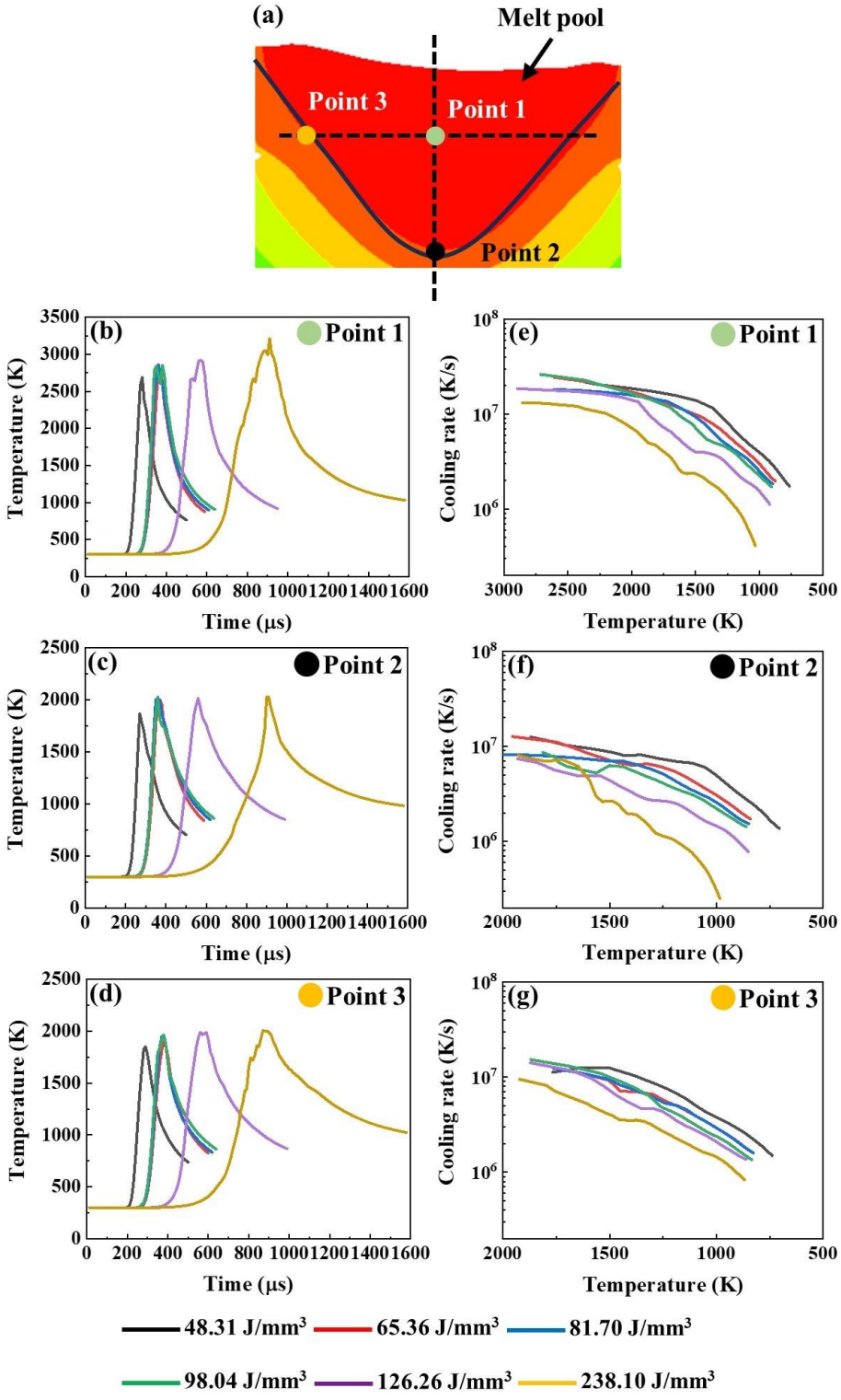

Fig. 16. Temperature variation in the different regions of melt pools, (a) schematic diagram of the measurement points in melt pools, (b)-(d) temperature varied with time, (e)-(g) cooling rate during the cooling process.

4.3 Effect of melting modes on the tensile properties

Results in sections 3.4 and 3.5 suggest that the tensile properties of printed material vary with the melting modes and VEDs. These variations are believed to be related to the different as-printed microstructure and dislocation densities [17, 19, 20, 62].

For L-PBF Ni, since the alloy strengthening is negligible, fine grain strengthening and dislocation strengthening can be considered the primary factors influencing the resistance to yield deformation [33, 63-65]. According to the Hall-Petch relationship, the coarser grains observed in the keyhole mode would normally associate with a lower strength [33, 63]. On the other hand, the high dislocation density observed in the keyhole mode would retard or block the movement of newly formed dislocations introduced via tensile deformation, which helps to strengthen the material [64, 65]. As a combined result, the keyhole mode material maintains a relatively good strength, as shown in Table. 4. Meanwhile, coarse grains and the lack of GNDs in the central areas of the melt pool provide a longer slip distance to accommodate plastic deformation [66]. Therefore, higher ductility is observed in the material printed under the keyhole mode.

Furthermore, it should also be pointed out that the samples fabricated under conduction mode exhibit a lower RD because of the lack of fusion defects induced at the low VED. There is a visible difference on the fracture surface between the two modes. Although some ductile dimples can be identified for the conduction mode, the fracture surface predominantly exhibits distinct cracks and cleavage characteristics, as shown in Fig. 17(a) and (b), indicating a brittle fracture here [19, 28]. In contrast, ductile dimples cover a large portion of the keyhole mode fracture surface, as shown in Fig. 17(c)-(h). The observed fracture surface corresponds well with the tensile results; brittle fracture indicates the samples printed under the conduction mode should have a lower ductility than those printed under the keyhole mode.

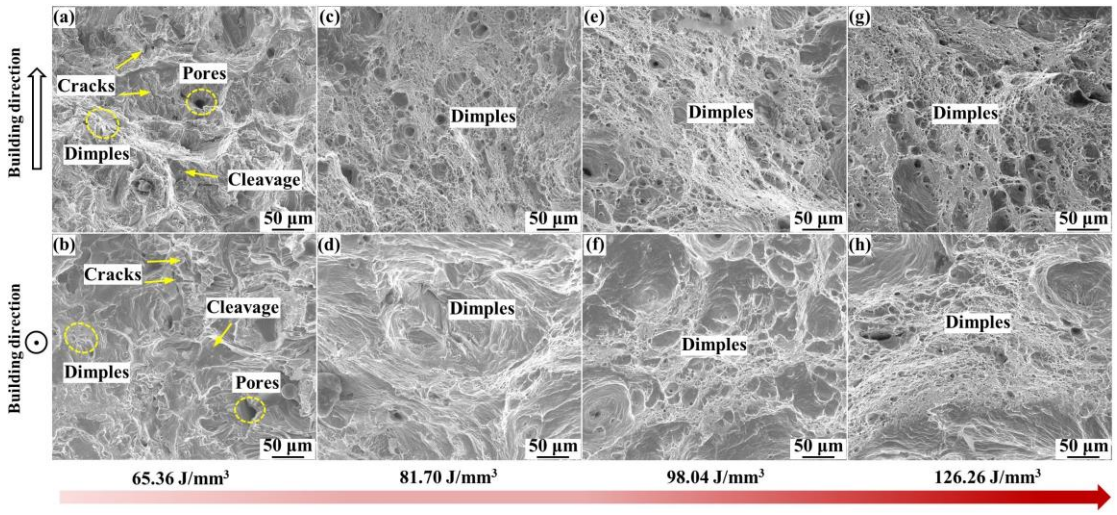

Fig. 17. Facture morphology of tensile specimens under conduction mode, (a) (c) (e) (g) parallel to building direction, (b) (d) (f) (h) perpendicular to building direction.

In addition, the grain size and dislocation density on the top surface (XY) are apparently different from those on the side surface (YZ). The top surface presents not only a high grain boundary density due to the small grain size but also large GNDs, leading to a higher strength for the samples printed perpendicular to the building direction than those printed parallel to the building direction [22, 64]. Moreover, it is evident that the anisotropic properties are prominent under the keyhole mode. This is attributed to the strong textures formed under the high VEDs, resulting in an intensified preferred orientation of the columnar grains. This intensified orientation contributes to a more obvious difference between the grain sizes of the two surfaces [67].

In summary, a keyhole mode melt pool is preferred to form during the L-PBF process of Ni. Samples printed in keyhole mode present better relative density than in conduction mode. In addition, the keyhole mode not only achieves an elongation comparable to or better than the casting sample but also obtains excellent strength. Different from the elemental segregation under keyhole mode in L-PBF Ni alloys, which is detrimental to strength [16-18], higher dislocation in L-PBF Ni under keyhole mode helps to promote the obtained strength. Although the conduction mode cam also presents a similar strength due to fine grain strengthening, its elongation is unsatisfactory. Therefore, the keyhole mode is considered more suitable for L-PBF Ni.

In this work, we demonstrated that VED is a tool that can effectively optimize printing results. The optimized printed material achieved a balanced strength and ductility, making it a good candidate for heat sinks and protection devices for electronic applications. Furthermore, since VED is a potent tool to control the print outcomes, it can be applied further to adjust the printed material's wear and corrosion resistance.

5. Conclusions

In this study, L-PBF Ni was printed via various volumetric energy densities under different melting modes. The corresponding microstructural features and tensile properties were experimentally characterized. The thermodynamics in the different melt pools were investigated via FEA, and the thermodynamics associated relationship between the applied VED and the obtained microstructure and tensile properties were discussed. The results and corresponding analysis demonstrate that:

(1) During the L-PBF printing, a peak temperature above the boiling point of Ni was achieved in the melt pool under a wide range of applied VEDs. Such a high temperature promoted the tendency to form keyhole mode rather than conduction mode during the L-PBF printing of Ni. Moreover, the keyhole mode provided a larger process window for printing near-full density L-PBF Ni compared to the conduction mode, suggesting better densification performance.

(2) The larger size of the keyhole mode melt pools resulted in a thermal gradient distribution that differs significantly from that in conduction mode. This led to an intensified <101> texture and cellular subgrains in the central zone of melt pools. Meanwhile, the conduction mode exhibited a week <001> texture, and the melt pool was filled with columnar subgrains.

(3) The cooling rate in the keyhole mode melt pool is lower than that in the conduction mode. This slower cooling rate contributed to the coarsening of subgrains and columnar grains, while increasing the fraction of uniformly deformed area.

(4) Due to the different thermodynamics, the keyhole mode microstructure exhibited a higher dislocation density, including both the density of GNDs and SSDs, than the conduction mode. With a higher VED located in the keyhole mode region, the GNDs were mainly concentrated around the grain and melt pool boundary. Meanwhile, the GNDs were evenly distributed in the conduction mode microstructure.

(5) The interaction between grain morphology, dislocation density, and distribution governed the

tensile performance of L-PBF Ni. The material printed in the keyhole mode can deliver an excellent combination of strength and ductility exceeding that of cast counterparts.

Declaration of competing interest

The authors declare that they have no known competing financial interests or personal relationships that could have appeared to influence the work reported in this paper.

Acknowledgments

This work was financially supported by the Scientific and Technological Innovation Foundation of Foshan (BK21BE015).

Reference

[1] K. Xu, B. Wu, J. Wan, Y. Li, M. Li. A potentiometric phosphate ion sensor based on electrochemically modified nickel electrode. Electrochim Acta 2022;412:140065. https://doi.org/10.1016/j.electacta.2022.140065.

[2] K. Wang, L. Jiang, X. Ye, J. Liang, C. Li, F. Liu, Z. Li. Absorption effect of pure nickel on the corrosion behaviors of the GH3535 alloy in tellurium vapor. Nucl Sci Tech 2021;32(12):140. https://doi.org/10.1007/s41365-021-00976-x.

[3] A. Romero, G. Herranz, A.L. Morales. Study of magnetoelastic properties of pure nickel parts produced by metal injection moulding. Mater. Des. 2015;88:438-445. https://doi.org/https://doi.org/10.1016/j.matdes.2015.08.137.

[4] T.R. Lee, C.P. Chang, P.W. Kao. The tensile behavior and deformation microstructure of cryo-rolled and annealed pure nickel. Mater. Sci. Eng. A 2005;408(1):131-135. https://doi.org/https://doi.org/10.1016/j.msea.2005.07.045.

[5] X. Zhang, C.J. Yocom, B. Mao, Y. Liao. Microstructure evolution during selective laser melting of metallic materials: A review. J Laser Appl 2019;31(3):031201. https://doi.org/10.2351/1.5085206.

[6] M. Chen, S. Van Petegem, Z. Zou, M. Simonelli, Y.Y. Tse, C.S.T. Chang, M.G. Makowska, D. Ferreira Sanchez, H. Moens-Van Swygenhoven. Microstructural engineering of a dual-phase Ti-Al-V-Fe alloy via in situ alloying during laser powder bed fusion. Addit Manuf 2022;59:103173. https://doi.org/10.1016/j.addma.2022.103173.

[7] H. Zhou, H. Su, Y. Guo, P. Yang, Y. Liu, Z. Shen, D. Zhao, H. Liu, T. Huang, M. Guo, J. Zhang, L. Liu, H. Fu. Formation and evolution mechanisms of pores in Inconel 718 during selective laser melting: Meso-scale modeling and experimental investigations. J Manuf Process 2022;81:202-213. https://doi.org/10.1016/j.jmapro.2022.06.072.

[8] P. Zuo, S. Chen, M. Wei, L. Zhou, J. Liang, C. Liu, M. Wang. Microstructure evolution of 24CrNiMoY alloy steel parts by high power selective laser melting. J Manuf Process 2019;44:28-37. https://doi.org/10.1016/j.jmapro.2019.05.037.

[9] Z. Zhang, T. Yuan, R. Li. Corrosion performance of selective laser-melted equimolar CrCoNi medium-entropy alloy vs its cast counterpart in 3.5 wt% NaCl. J Alloy Compd 2021;864:158105. https://doi.org/10.1016/j.jallcom.2020.158105.

[10] B. Li, W. Fu, H. Xu, B. Qian, F. Xuan. Additively manufactured Ni-15Fe-5Mo Permalloy via selective laser melting and subsequent annealing for magnetic-shielding structures: Process, micro-structural and soft-magnetic characteristics. J Magn Magn Mater 2020;494:165754. https://doi.org/10.1016/j.jmmm.2019.165754.

[11] T. Yue, S. Zhang, C. Wang, W. Xu, Y. Xu, Y. Shi, Y. Zang. Effects of selective laser melting parameters on surface quality and densification behaviours of pure nickel. T Nonferr Metal Soc 2022;32(8):2634-2647. https://doi.org/10.1016/s1003-6326(22)65972-7.

[12] C.Y. Yap, H.K. Tan, Z. Du, C.K. Chua, Z. Dong. Selective laser melting of nickel powder. Rapid Prototyp J 2017;23(4):750-757. https://doi.org/10.1108/rpj-01-2016-0006.

[13] Y. Zhao, G.R. Zhao, W.Y. Ma, L. Zheng, M. Liu. Study on process, structure, and properties of nickel selective laser melting. Laser Optoelectron P 2020;57(17):171402. https://doi.org/10.3788/lop57.171402.

[14] A.R. Yan, T.T. Yang, Y.L. Wang, Z.H. Ma, Y. Du, Z.Y. Wang. Thermal properties and mechanical properties of selective laser melting different layer thicknesses of Ni powder. Chin. J. Lasers 2016;43(2):0203004. https://doi.org/10.3788/cjl201643.0203004.

[15] H. Torbati-Sarraf, I. Ghamarian, B. Poorganji, S.A. Torbati-Sarraf. An Investigation on the role of crystallographic texture on anisotropic electrochemical behavior of a commercially pure nickel manufactured by laser powder bed fusion (L-PBF) additive manufacturing. Electrochim Acta 2020;354:136694. https://doi.org/10.1016/j.electacta.2020.136694.
[16] T. Guraya, S. Singamneni, Z.W. Chen. Microstructure formed during selective laser melting of IN738LC in keyhole mode. J Alloy Compd 2019;792:151-160. https://doi.org/10.1016/j.jallcom.2019.03.419.
[17] L. Zhang, Y. Li, S. Zhang, Q. Zhang. Selective laser melting of IN738 superalloy with a low Mn+Si content: Effect of energy input on characteristics of molten pool, metallurgical defects, microstructures and mechanical properties. Mater. Sci. Eng. A 2021;826:141985. https://doi.org/10.1016/j.msea.2021.141985.
[18] H. Yang, J. Yang, W. Huang, Z. Wang, X. Zeng. The printability, microstructure, crystallographic features and microhardness of selective laser melted Inconel 718 thin wall. Mater. Des. 2018;156:407-418. https://doi.org/10.1016/j.matdes.2018.07.007.
[19] M. Salarian, H. Asgari, M. Vlasea. Pore space characteristics and corresponding effect on tensile properties of Inconel 625 fabricated via laser powder bed fusion. Mater. Sci. Eng. A 2020;769:138525. https://doi.org/10.1016/j.msea.2019.138525.
[20] H. Yan, G. Zhu, H. Shi, P. Zhang, H. Li, Q. Lu, Z. Li. Microstructure and mechanical properties of K438 alloy processed by selective laser melting and subsequent heat treatment. Mater Charact 2022;191:112116. https://doi.org/10.1016/j.matchar.2022.112116.
[21] Y. Li, M. Založnik, J. Zollinger, L. Dembinski, A. Mathieu. Effects of the powder, laser parameters and surface conditions on the molten pool formation in the selective laser melting of IN718. J Mater Process Techn 2021;289:116930. https://doi.org/10.1016/j.jmatprotec.2020.116930.
[22] E. Hug, M. Leli`evre, C. Folton, A. Ribet, M. Martinez-Celis, C.e. Keller. Additive manufacturing of a Ni-20 wt%Cr binary alloy by laser powder bed fusion: impact of the microstructure on the mechanical properties. Mater. Sci. Eng. A 2022;834:142625. https://doi.org/10.1016/j.msea.2022.142625.
[23] C. Guo, Z. Xu, Y. Zhou, S. Shi, G. Li, H. Lu, Q. Zhu, R.M. Ward. Single-track investigation of IN738LC superalloy fabricated by laser powder bed fusion: Track morphology, bead characteristics and part quality. J Mater Process Technol 2021;290:117000. https://doi.org/10.1016/j.jmatprotec.2020.117000.
[24] A.E. Hassanin, F. Scherillo, U. Prisco, R. Sansone, A. Astarita. Selective laser melting of Cu-inconel 718 powder mixtures. J Manuf Process 2020;59:679-689. https://doi.org/10.1016/j.jmapro.2020.10.039.
[25] T. Yue, Z. Zou, S. Zhang, Y. Xu, Y. Zang. Influence of volumetric energy density on the tribological behaviors of pure nickel fabricated by laser powder bed fusion. Virtual Phys Prototyp 2023;18(1):1-20. https://doi.org/10.1080/17452759.2023.2262449.
[26] M. Ghayoor, K. Lee, Y. He, C.-h. Chang, B.K. Paul, S. Pasebani. Selective laser melting of 304L stainless steel: Role of volumetric energy density on the microstructure, texture and mechanical properties. Addit Manuf 2020;32:101011. https://doi.org/10.1016/j.addma.2019.101011.
[27] J. Zhang, B. Song, Q. Wei, D. Bourell, Y. Shi. A review of selective laser melting of aluminum alloys: Processing, microstructure, property and developing trends. J Mater Sci Technol 2019;35(2):270-284. https://doi.org/10.1016/j.jmst.2018.09.004.
[28] B. AlMangour, M. Luqman, D. Grzesiak, H. Al-Harbi, F. Ijaz. Effect of processing parameters

on the microstructure and mechanical properties of Co–Cr–Mo alloy fabricated by selective laser melting. Mater. Sci. Eng. A 2020;792:139456. https://doi.org/10.1016/j.msea.2020.139456.
[29] G. Jing, W. Huang, H. Yang, Z. Wang. Microstructural evolution and mechanical properties of 300M steel produced by low and high power selective laser melting. J Mater Sci Technol 2020;48:44-56. https://doi.org/10.1016/j.jmst.2019.12.020.
[30] H. Wu, Y. Ren, J. Ren, L. Liang, R. Li, Q. Fang, A. Cai, Q. Shan, Y. Tian, I. Baker. Selective laser melted AlSi10Mg alloy under melting mode transition: Microstructure evolution, nanomechanical behaviors and tensile properties. J Alloy Compd 2021;873:159823. https://doi.org/10.1016/j.jallcom.2021.159823.
[31] J. Yang, J. Han, H. Yu, J. Yin, M. Gao, Z. Wang, X. Zeng. Role of molten pool mode on formability, microstructure and mechanical properties of selective laser melted Ti-6Al-4V alloy. Mater. Des. 2016;110:558-570. https://doi.org/10.1016/j.matdes.2016.08.036.
[32] H. Wu, Y. Ren, J. Ren, A. Cai, M. Song, Y. Liu, X. Wu, Q. Li, W. Huang, X. Wang, I. Baker. Effect of melting modes on microstructure and tribological properties of selective laser melted AlSi10Mg alloy. Virtual Phys Prototyp 2020;15(sup1):570-582. https://doi.org/10.1080/17452759.2020.1811932.
[33] J. Lu, X. Lin, N. Kang, Y. Cao, Q. Wang, W. Huang. Keyhole mode induced simultaneous improvement in strength and ductility of Sc modified Al–Mn alloy manufactured by selective laser melting. Mater. Sci. Eng. A 2021;811:141089. https://doi.org/10.1016/j.msea.2021.141089.
[34] K. Karayagiz, L. Johnson, R. Seede, V. Attari, B. Zhang, X. Huang, S. Ghosh, T. Duong, I. Karaman, A. Elwany, R. Arróyave. Finite interface dissipation phase field modeling of Ni–Nb under additive manufacturing conditions. Acta Mater. 2020;185:320-339. https://doi.org/10.1016/j.actamat.2019.11.057.
[35] S. Patel, M. Vlasea. Melting modes in laser powder bed fusion. Materialia 2020;9:100591. https://doi.org/10.1016/j.mtla.2020.100591.
[36] M. Guo, D. Gu, L. Xi, H. Zhang, J. Zhang, J. Yang, R. Wang. Selective laser melting additive manufacturing of pure tungsten: Role of volumetric energy density on densification, microstructure and mechanical properties. Int J Refract Met H 2019;84:105025. https://doi.org/10.1016/j.ijrmhm.2019.105025.
[37] D. Daia, D. Gu, Q. Ge, Y. Li, X. Shi, Y. Sun, S. Li. Mesoscopic study of thermal behavior, fluid dynamics and surface morphology during selective laser melting of Ti-based composites. Comput. Mater. Sci. 2020;177:109598. https://doi.org/10.1016/j.commatsci.2020.109598.
[38] W. Yuan, H. Chen, T. Cheng, Q. Wei. Effects of laser scanning speeds on different states of the molten pool during selective laser melting: Simulation and experiment. Mater. Des. 2020;189:108542. https://doi.org/10.1016/j.matdes.2020.108542.
[39] P. Jin, Q. Tang, K. Li, Q. Feng, Z. Ren, J. Song, Y. Nie, S. Ma. The relationship between the macro- and microstructure and the mechanical properties of selective-laser-melted Ti6Al4V samples under low energy inputs: Simulation and experiment. Opt Laser Technol 2022;148:107713. https://doi.org/10.1016/j.optlastec.2021.107713.
[40] Z. Sun, Y.-H. Chueh, L. Li. Multiphase mesoscopic simulation of multiple and functionally gradient materials laser powder bed fusion additive manufacturing processes. Addit Manuf 2020;35. https://doi.org/10.1016/j.addma.2020.101448.
[41] T. Qi, H. Zhu, H. Zhang, J. Yin, L. Ke, X. Zeng. Selective laser melting of Al7050 powder: Melting mode transition and comparison of the characteristics between the keyhole and conduction

mode. Mater. Des. 2017;135:257-266. https://doi.org/10.1016/j.matdes.2017.09.014.
[42] T. DebRoy, H.L. Wei, J.S. Zuback, T. Mukherjee, J.W. Elmer, J.O. Milewski, A.M. Beese, A. Wilson-Heid, A. De, W. Zhang. Additive manufacturing of metallic components – Process, structure and properties. Prog Mater Sci 2018;92:112-224. https://doi.org/10.1016/j.pmatsci.2017.10.001.
[43] T. Wang, S. Dai, H. Liao, H. Zhu. Pores and the formation mechanisms of SLMed AlSi10Mg. Rapid Prototyping J 2020;26(9):1657-1664. https://doi.org/10.1108/rpj-02-2020-0036.
[44] X. Zhang, Z. Xiao, W. Yu, C.K. Chua, L. Zhu, Z. Wang, P. Xue, S. Tan, Y. Wu, H. Zheng. Influence of erbium addition on the defects of selective laser-melted 7075 aluminium alloy. Virtual Phys Prototyp 2021;17(2):406-418. https://doi.org/10.1080/17452759.2021.1990358.
[45] C. Wang, X. Tan, E. Liu, S.B. Tor. Process parameter optimization and mechanical properties for additively manufactured stainless steel 316L parts by selective electron beam melting. Mater. Des. 2018;147:157-166. https://doi.org/10.1016/j.matdes.2018.03.035.
[46] S. Staroń, B. Dubiel, K. Gola, I. Kalemba-Rec, M. Gajewska, H. Pasiowiec, R. Wróbel, C. Leinenbach. Quantitative Microstructural Characterization of Precipitates and Oxide Inclusions in Inconel 625 Superalloy Additively Manufactured by L-PBF Method. Metall Mater Trans A 2022;53(7):2459-2479. https://doi.org/10.1007/s11661-022-06679-1.
[47] S.-H. Li, Y. Zhao, P. Kumar, U. Ramamurty. Effect of initial dislocation density on the plastic deformation response of 316L stainless steel manufactured by directed energy deposition. Mater. Sci. Eng. A 2022;851:143591. https://doi.org/10.1016/j.msea.2022.143591.
[48] P. Deng, M. Karadge, R.B. Rebak, V.K. Gupta, B.C. Prorok, X. Lou. The origin and formation of oxygen inclusions in austenitic stainless steels manufactured by laser powder bed fusion. Addit Manuf 2020;35:101334. https://doi.org/10.1016/j.addma.2020.101334.
[49] C. Wang, D. Chen, Y. Zhou, Z. Xie, Q. Fang, S. Wen, C. Yan. Microstructures, Thermal and Mechanical Properties of Pure Tungsten—A Comparison Between Selective Laser Melting and Hot Rolling. Chin J Mech Eng-En 2022;35(1):1-8. https://doi.org/10.1186/s10033-022-00712-5.
[50] A. Rezaei, R. Mahmudi, C. Cayron, R.E. Loge. Superplastic behavior of a severely deformed Mg–6Gd−3Y−0.5Ag alloy. Mater. Sci. Eng. A 2021;802:140616. https://doi.org/10.1016/j.msea.2020.140616.
[51] O. Rezvanian, M.A. Zikry, A.M. Rajendran. Statistically stored, geometrically necessary and grain boundary dislocation densities: microstructural representation and modelling. Proc. Math. Phys. Eng. Sci. 2007;463(2087):2833-2853. https://doi.org/10.1098/rspa.2007.0020.
[52] L. Cui, C.-H. Yu, S. Jiang, X. Sun, R.L. Peng, J.-E. Lundgren, J. Moverare. A new approach for determining GND and SSD densities based on indentation size effect: An application to additive-manufactured Hastelloy X. J Mater Sci Technol 2022;96:295-307. https://doi.org/10.1016/j.jmst.2021.05.005.
[53] Y. Xiang, X. Wang, H. Shi, X. Hu, C. Xu, Q. Zhang. Decipher the ultra-high strengthening and toughening efficiency of GNS-MgO/Mg layered composite with in-situ enhanced interface. Carbon 2022;196:783-794. https://doi.org/10.1016/j.carbon.2022.04.063.
[54] Q. Yang, D.L. Cheng, J. Liu, L. Wang, Z. Chen, M.L. Wang, S.Y. Zhong, Y. Wu, G. Ji, H.W. Wang. Microstructure evolution of the TiB2/Al composites fabricated by powder metallurgy during hot extrusion. Mater Charact 2019;155:109834. https://doi.org/10.1016/j.matchar.2019.109834.
[55] C.L. Wu, W. Zai, H.C. Man. Additive manufacturing of ZK60 magnesium alloy by selective laser melting: Parameter optimization, microstructure and biodegradability. Mater. Today Commun. 2021;26:101922. https://doi.org/10.1016/j.mtcomm.2020.101922.

[56] W.E. King, H.D. Barth, V.M. Castillo, G.F. Gallegos, J.W. Gibbs, D.E. Hahn, C. Kamath, A.M. Rubenchik. Observation of keyhole-mode laser melting in laser powder-bed fusion additive manufacturing. J Mater Process Techn 2014;214(12):2915-2925. https://doi.org/10.1016/j.jmatprotec.2014.06.005.
[57] C. Zhao, Y. Bai, Y. Zhang, X. Wang, J.M. Xue, H. Wang. Influence of scanning strategy and building direction on microstructure and corrosion behaviour of selective laser melted 316L stainless steel. Mater. Des. 2021;209:109999. https://doi.org/10.1016/j.matdes.2021.109999.
[58] J.J. Marattukalam, D. Karlsson, V. Pacheco, P. Beran, U. Wiklund, U. Jansson, B. Hjörvarsson, M. Sahlberg. The effect of laser scanning strategies on texture, mechanical properties, and site-specific grain orientation in selective laser melted 316L SS. Mater. Des. 2020;193:108852. https://doi.org/10.1016/j.matdes.2020.108852.
[59] H. Yang, Y. Zhu, Y. Yang. Enhancing Wear Resistance of Selective Laser Melted Parts: Influence of Energy Density. J Tribol-T Asme 2020;142(11):111701. https://doi.org/10.1115/1.4047297.
[60] T. Yang, T. Liu, W. Liao, E. MacDonald, H. Wei, X. Chen, L. Jiang. The influence of process parameters on vertical surface roughness of the AlSi10Mg parts fabricated by selective laser melting. J Mater Process Technol 2019;266:26-36. https://doi.org/10.1016/j.jmatprotec.2018.10.015.
[61] S. Wen, C. Wang, Y. Zhou, L. Duan, Q. Wei, S. Yang, Y. Shi. High-density tungsten fabricated by selective laser melting: Densification, microstructure, mechanical and thermal performance. Opt Laser Technol 2019;116:128-138. https://doi.org/10.1016/j.optlastec.2019.03.018.
[62] H. Wang, L. Wang, R. Cui, B. Wang, L. Luo, Y. Su. Differences in microstructure and nano-hardness of selective laser melted Inconel 718 single tracks under various melting modes of molten pool. J. Mater. Res. Technol. 2020;9(5):10401-10410. https://doi.org/https://doi.org/10.1016/j.jmrt.2020.07.029.
[63] P. Gao, W. Huang, H. Yang, G. Jing, Q. Liu, G. Wang, Z. Wang, X. Zeng. Cracking behavior and control of β-solidifying Ti-40Al-9V-0.5Y alloy produced by selective laser melting. J. Mater. Res. Technol. 2020;39:144-154. https://doi.org/10.1016/j.jmst.2019.08.026.
[64] D. Lin, L. Xu, Y. Han, Y. Zhang, H. Jing, L. Zhao, F. Minami. Structure and mechanical properties of a FeCoCrNi high-entropy alloy fabricated via selective laser melting. Intermetallics 2020;127:106963. https://doi.org/10.1016/j.intermet.2020.106963.
[65] Y.H. Zhou, W.P. Li, D.W. Wang, L. Zhang, K. Ohara, J. Shen, T. Ebel, M. Yan. Selective laser melting enabled additive manufacturing of Ti–22Al–25Nb intermetallic: Excellent combination of strength and ductility, and unique microstructural features associated. Acta Mater 2019;173:117-129. https://doi.org/10.1016/j.actamat.2019.05.008.
[66] Z. Zou, M. Simonelli, J. Katrib, G. Dimitrakis, R. Hague. Microstructure and tensile properties of additive manufactured Ti-6Al-4V with refined prior-β grain structure obtained by rapid heat treatment. Mater. Sci. Eng. A 2021;814:141271. https://doi.org/https://doi.org/10.1016/j.msea.2021.141271.
[67] A. Rezaei, A. Rezaeian, A. Kermanpur, M. Badrossamay, E. Foroozmehr, M. Marashi, A. Foroozmehr, J. Han. Microstructural and mechanical anisotropy of selective laser melted IN718 superalloy at room and high temperatures using small punch test. Mater Charact 2020;162:110200. https://doi.org/10.1016/j.matchar.2020.110200.